

1 **The characteristics of the 2022 Tonga volcanic tsunami in the Pacific Ocean**

2 Gui Hu¹, Linlin Li^{1,2}, Zhiyuan Ren³, Kan Zhang¹

3 1. Guangdong Provincial Key Laboratory of Geodynamics and Geohazards, School of Earth Sciences
4 and Engineering, Sun Yat-sen University, Guangzhou, China

5 2. Southern Marine Science and Engineering Guangdong Laboratory (Zhuhai), Zhuhai, China

6 3. Department of Civil and Environmental Engineering, National University of Singapore, Singapore.

7 *Correspondence to:* Linlin Li (lilinlin3@mail.sysu.edu.cn)

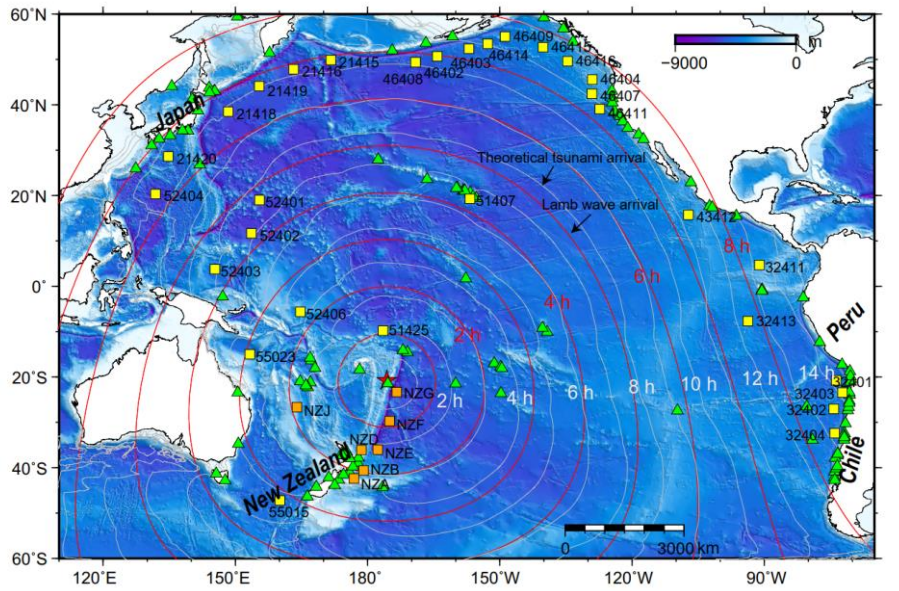
8 **Abstract.** On 15th January 2022, an exceptional eruption of Hunga Tonga–Hunga Ha’apai volcano
9 generated atmospheric and tsunami waves that were widely observed at oceans globally, gaining a
10 remarkable attention to scientists in related fields. The tsunamigenic mechanism of this rare event
11 remains an enigmatic due to its complexity and lacking of direct underwater observations. Here, to
12 explore the tsunamigenic mechanisms of this volcanic tsunami event and its hydrodynamic processes in
13 the Pacific Ocean, we conduct tsunami waveform and spectral analyses of the waveform recordings at
14 116 coastal gauges and 38 deep-ocean buoys across the Pacific Ocean. Combined with the constraints of
15 some representative barometers, we obtain the plausible tsunamigenic origins during the volcano activity.
16 We identify four distinct tsunami wave components generated by air-sea coupling and seafloor crustal
17 deformation. Those tsunami components are differentiated by their different propagating speeds or period
18 bands. The first-arriving tsunami component with ~80–100 min period was from shock waves spreading
19 at a velocity of ~1000 m/s in vicinity of the eruption. The second component with extraordinary tsunami
20 amplitude in deep sea was from Lamb waves. The Lamb wave with ~30–40 min period radically
21 propagated outward from the eruption site with spatially decreasing propagation velocities from ~340
22 m/s to ~315 m/s. The third component with ~10–30 min period was probably from some atmospheric
23 gravity wave modes propagating faster than 200 m/s but slower than Lamb waves. The last component
24 with ~3–5 min period originated from partial caldera collapse with dimension of ~0.8–1.8 km.
25 Surprisingly, the 2022 Tonga volcanic tsunami produced long oscillation in the Pacific Ocean which is
26 comparable with those of the 2011 Tohoku tsunami. We point out that the long oscillation is not only
27 associated with the resonance effect with the atmospheric acoustic-gravity waves, but more importantly
28 the interactions with local bathymetry. This rare event also calls for more attention to the tsunami hazards
29 produced by atypical tsunamigenic source, e.g., volcanic eruption.

30 **1. Introduction**

31 On 15 January 2022 at 04:14:45 (UTC), a submarine volcano erupted violently at the uninhabited Hunga
32 Tonga-Hunga Ha'apai (HTHH) island at 20.546°S 175.390°W (USGS, 2022). The volcano is located ~67
33 km north of Nuku'alofa, the capital of Tonga (NASA, 2022) (Figure 1). The blasts launched plumes of
34 ash, steam, and gas ~58 km high into stratosphere (Yuen et al., 2022) which not only blanketed nearby
35 islands in ash (Duncombe, 2022; NASA, 2022), but caused various atmospheric acoustic-gravity wave
36 modes (AGWs) of various scales, e.g., Lamb waves from atmospheric surface pressure disturbance
37 associated with the eruption (Liu and Higuera, 2022; Adam, 2022; Kubota et al., 2022; Matoza et al.,
38 2022). Tsunami with conspicuous sea level changes were detected by coastal tide gauges and Deep-ocean
39 Assessment and Reporting of Tsunamis (DART) buoy stations in the Pacific (Figure 1), the Atlantic, and
40 Indian Oceans as well as the Caribbean and Mediterranean seas (Carvajal et al., 2022; Kubota et al., 2022;
41 Ramírez-Herrera et al., 2022), while the large waves were mainly concentrated in the Pacific Ocean, like
42 coastlines of New Zealand, Japan, California, and Chile (Carvajal et al., 2022). The event caused at least
43 3 fatalities in Tonga. Two people drowned in northern Peru when ~2 m destructive tsunami waves
44 inundated an island in the Lambayeque region, Chile (Edmonds, 2022).

45 Satellite images revealed that the elevation of HTHH island has gone through dramatic change before
46 and after the mid-January 2022 eruption. Previously, after the 2015 eruption, the two existing Hunga
47 Tonga and Hunga Ha'apai Islands were linked together. The volcanic island rose 1.8 km from the seafloor
48 where it stretched ~20 km across and topped a underwater caldera ~5 km in diameter (Garvin et al., 2018;
49 NASA, 2022). After the violent explosion on 15 January 2022, the newly formed island during 2015 was
50 completely gone, with only small tips left in far southwestern and northeastern HTHH island (NASA,
51 2022). HTHH volcano lies along the northern part of Tonga-Kermadec arc, where the Pacific Plate
52 subducts under the Indo-Australian Plate (Billen et al., 2003). The convergence rate (15~24 cm/year)
53 between the Tonga-Kermadec subduction system and the Pacific plate is among the fastest recorded plate
54 velocity on Earth, forming the second deepest trench around the globe (Satake, 2010; Bevis et al., 1995).
55 The fast convergence rate contributes to the frequent earthquakes, tsunamis and volcanic eruptions in
56 this region historically (Bevis et al., 1995). The 2022 HTHH volcano is part of a submarine-volcano
57 chain that extends all the way from New Zealand to Fiji (Plank et al., 2020). HTHH volcano had many
58 notable eruptions before 2022 since its first historically recorded eruption in 1912, i.e., in 1937, 1988,

59 2009, 2014-2015 (Global Volcanism Program, <https://volcano.si.edu>).



60
61 **Figure 1. The spatial distribution of the eruption site (red star), DART stations (squares), tide**
62 **gauges (triangles) and the calculated tsunami arrival times. White contours indicate the modelled**
63 **arrival times of conventional tsunami. Red contours indicate the estimated arrival times of Lamb**
64 **waves (see how we derive these contours in section 3.1).**

65 The 2022 HTHH eruption is the first volcanic event which generates worldwide tsunami signatures since
66 the 1883 Krakatau event (Matoza et al., 2022; Self and Rampino, 1981; Nomanbhoy and Satake, 1995).
67 The tsunamigenic mechanism of this rare volcanic eruption-induced tsunami is still poorly understood
68 due to its complex nature and the deficiencies of near-field seafloor surveys. Various tsunami generation
69 mechanisms have been proposed so far based on the observations of ground-based and spaceborne
70 geophysical instrumentations (Kubota et al., 2022; Matoza et al., 2022; Carvajal et al., 2022). The
71 mechanisms are closely associated with the air-sea coupling with atmospheric waves. Atmospheric
72 waves propagating in the atmospheric fluid are generated by different physical mechanisms (Gossard
73 and Hooke, 1975a). Lamb wave is a horizontally propagating acoustic waves in Lamb mode
74 which is trapped at the earth's surface with group velocities close to the mean sound velocity of
75 the lower atmosphere (e.g. Lamb, 1932). Atmospheric gravity wave is triggered when air
76 molecules in the atmosphere are disturbed vertically other than horizontally (e.g. Le Pichon et
77 al., 2010). Nonlinear propagation of atmospheric wave may cause period lengthening and the

78 formation of shock-wave (Matoza et al., 2022). The most-mentioned mechanism of the tsunami is
79 the fast-traveling atmospheric Lamb wave generated by the atmospheric pressure rise of ~2 hPa during
80 the eruption. The Lamb wave circled the Earth for several times with travelling speed close to that of the
81 sound wave in the lower atmosphere, leading to globally observed sea level fluctuations (Adam, 2022;
82 Duncombe, 2022; Kubota et al., 2022; Matoza et al., 2022) (Figure 1). The second mechanism is
83 suggested to be a variety of other acoustic-gravity wave modes (Adam, 2022; Matoza et al., 2022;
84 Themens et al., 2022; Zhang et al., 2022). The third mechanism may be related to the seafloor crustal
85 deformation induced by one or more volcanic activities in the vicinity of the eruption site (e.g.,
86 pyroclastic flows, partial collapse of the caldera) (Carvajal et al., 2022), which are more responsible for
87 the near-field tsunamis with theoretical tsunami speeds.

88 To investigate the possible tsunamigenic mechanisms and detailed hydrodynamic behaviors of this rare
89 volcanic tsunami event, in this study, we collect, process and analyze the sea level measurements from
90 116 tide gauge and 38 DART buoys in the Pacific Ocean (shown in Figures 1 and 2). We first do statistical
91 analysis of the tsunami waveforms to estimate the propagating speed of the Lamb wave and to understand
92 the tsunami wave characteristics in the Pacific Ocean through demonstrating the tsunami wave properties,
93 i.e., arrival times, wave heights and durations. We then conduct wavelet analysis for representative DART
94 buoys and tide gauges respectively to explore tsunamigenic mechanisms of the event and to better
95 understand its hydrodynamic processes in the Pacific Ocean. Aided by wavelet analysis of corresponding
96 barometers near the selected DART buoys and comparison with tsunami records of the 2011 Tohoku
97 tsunami, we are able to piece together all the analysis and demonstrate that the 2022 HTHH tsunami was
98 generated by air-sea coupling with a wide range of atmospheric waves with different propagating
99 velocities and period bands, and seafloor crustal deformation associated with the volcanic eruption. We
100 demonstrate as well that the tsunami was amplified at the far-field Pacific coastlines where the local
101 bathymetric effects play a dominant role in tsunami scale.

102 **2. Data and Methods**

103 **2.1 Data**

104 We collected high-quality sea level records across the Pacific Ocean at 38 DART buoys (in which 31
105 stations from <https://nctr.pmel.noaa.gov/Dart/>, 7 stations from <https://tilde.geonet.org.nz/dashboard/>) and

106 116 tide gages from IOC (The Intergovernmental Oceanographic Commission, <http://www.ioc-sealevelmonitoring.org>) (Figure 1). The epicentral distances of tide gauges and DART buoys range
107 between 74–10790 km and 375–10414 km, respectively. The sampling rates of DART buoys are
108 changing over time. Passing of tsunami event generally can trigger the DART system to enter its high
109 frequency sampling mode (15 seconds or 1 min) from normal frequency mode (15 min)
110 (www.ndbc.noaa.gov/dart). In contrast, sampling rates of normal tide gauges at coasts are uniform with
111 sampling interval of 1 min. The sampling interval of both DART and tide gauges is preprocessed to 15
112 seconds. Firstly, we eliminate abnormal spikes and fill gaps by linear interpolation. Secondly, we applied
113 a fourth-order Butterworth-Highpass filter with a cut-off frequency of 3.5 e-5 Hz (~ 8 hours) to remove
114 the tidal components (Figure 2) (Heidarzadeh and Satake, 2013). After the two steps, quality control step
115 is conducted to select high-quality data, in which we delete waveforms with spoiled data or massive data
116 loss due to equipment failure, or with the maximum tsunami heights of tide gauges less than 0.2 m, then
117 the selected data will be ready for further statistics and spectral analysis. We also collect and analyze the
118 atmospheric pressure disturbance data recorded by some representative barometers. The sampling rates
119 of the barometers is generally uniform with a sampling rate of 1 min except for some stations in New
120 Zealand with interval of 10 min. Considering the sample rate, we employ a fourth-order Butterworth-
121 Bandpass filter with period ranging between 2–150 min for wavelet analysis of the barometers with 1
122 min sample rate, while we apply the fourth-order Butterworth-Bandpass filter with range of 30–150 min
123 to long-period waveform display based on two reasons. (1) The barometer data we use for the analysis
124 include some in New Zealand with 10 min sample rate; (2) Filtering out the short-period waves helps
125 highlight long-period tsunami wave components.
126
127 The tsunami waveforms recorded by DART buoys which are installed offshore in the deep water are
128 expected to contain certain characteristics of the tsunami source (Wang et al., 2020, 2021). The
129 waveforms recorded by tide gauge distributed along coastlines are significantly influenced by local
130 bathymetry/topography which are used for investigating bathymetric effect on tsunami behaviors
131 (Rabinovich et al., 2017, 2006; Rabinovich, 2009). Therefore, we use the DART data for source-related
132 analysis and choose some tide gauge data to investigate the tsunami behaviors at the Pacific coastlines.
133

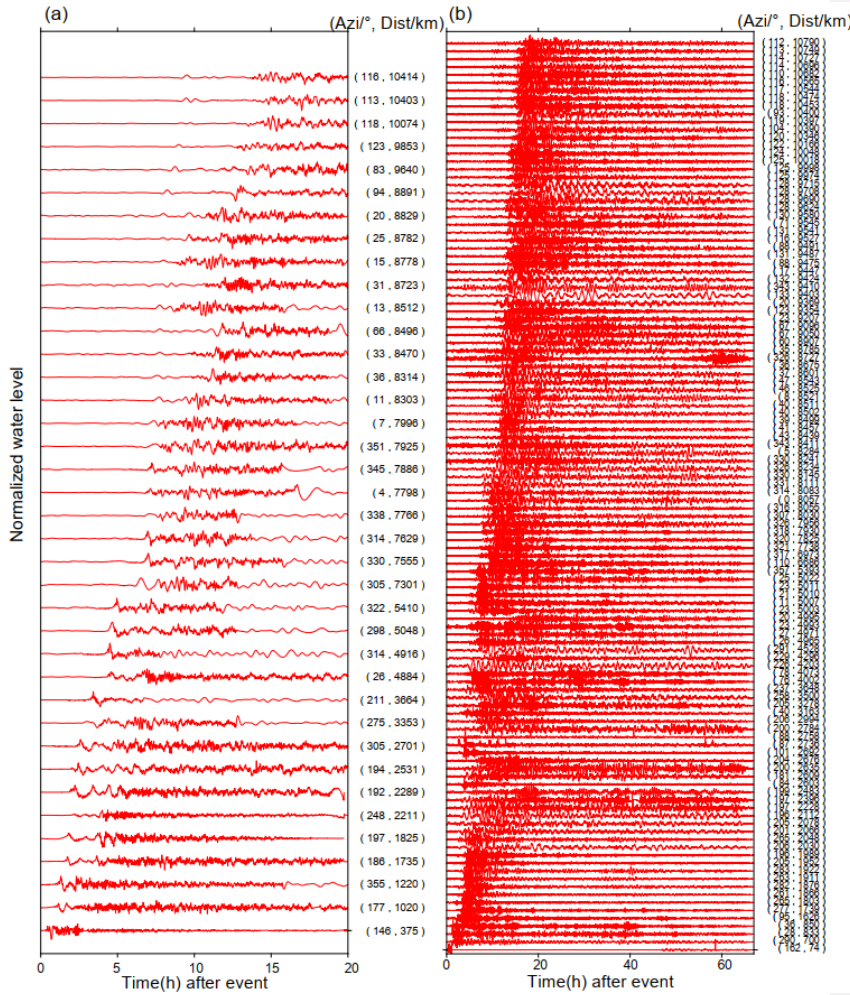


Figure 2. Detided tsunami waveforms at (a) DART buoys and (b) tide gauges. Waveforms in both subplots are shown in ascending distance. Azi stands for azimuth. The data are normalized with respect to the largest amplitude of each tide gauge.

2.2 Tsunami Modelling

We use a numerical tsunami modelling package JAGURS (Baba et al. 2015) to simulate the tsunami propagation of the 2022 HTHH event and obtain the theoretical tsunami arrival time based on the shallow water wave speed (white contours in Figure 1). The code solves linear Boussinesq-type equations in a spherical coordinate system using a finite difference approximation with the leapfrog method. We specify a unit Gaussian-shaped vertical sea surface displacement at the volcanic base as the source of

144 conventional tsunami. For a unite source i with center at longitude φ_i and latitude θ_i , the
145 displacement distribution $Zi(\varphi, \theta)$ can be expressed as:

$$146 Zi(\varphi, \theta) = \exp\left[-\frac{(\varphi-\varphi_i)^2 + (\theta-\theta_i)^2}{2\sigma^2}\right] \quad (1)$$

147 Where we set characteristic length σ as 5 km (NASA, 2022). The bathymetric data is resampled from the
148 GEBCO 2019 with 15 arc-sec resolution (The General Bathymetric Chart of the Oceans, downloaded
149 from <https://www.gebco.net>).

150 **2.3 Spectral Analysis of Tsunami Waves**

151 To investigate the temporal changes of the dominant wave periods, we conduct continuous wavelet
152 transformation (frequency-time) analyses for some representative DART buoys, tide gauges and
153 barometers, in which wavelet Morlet mother function is implemented (Kristeková et al., 2006). The first
154 32-hour time series of DART buoys and barometers after the eruption (at 04:14:45 on 15 January 2022)
155 are used for source-related wavelet analysis. The first 48-hour time series of tide gauges after the eruption
156 are employed for hydrodynamics-related wavelet analysis at coastlines. We adopt the Averaged-Root-
157 Mean-Square (ARMS) method as a measure of absolute average tsunami amplitude with a moving time
158 window of 20 min to calculate the tsunami duration (Heidarzadeh and Satake, 2014). We define the time
159 durations as the time period where ARMS levels of tsunami waves are above those prior to the tsunami
160 arrivals.

161 **3. Results**

162 **3.1 The decreasing propagation velocities of the Lamb Wave**

163 Although many types of atmospheric waves were generated by the 2022 HTHH eruption, the most
164 prominent signature was the Lamb waves which were globally observed by ground-based and spaceborne
165 geophysical instrumentations (Kulichkov et al., 2022; Liu et al., 2022; Lin et al., 2022; Matoza et al.,
166 2022; Themens et al., 2022; Adam, 2022; Kubota et al., 2022). Interestingly, we notice that a wide range
167 of the velocities from 280 m/s to 340 m/s were proposed through observations and Lamb wave modelling
168 (e.g., Kubota et al., 2022; Lin et al., 2022; Matoza et al., 2022; Themens et al., 2022). The travelling
169 velocity of Lamb waves in real atmosphere is affected by temperature distributions, winds and dissipation
170 (Otsuka, 2022). To investigate whether the propagation speeds of the lamb wave change in space and

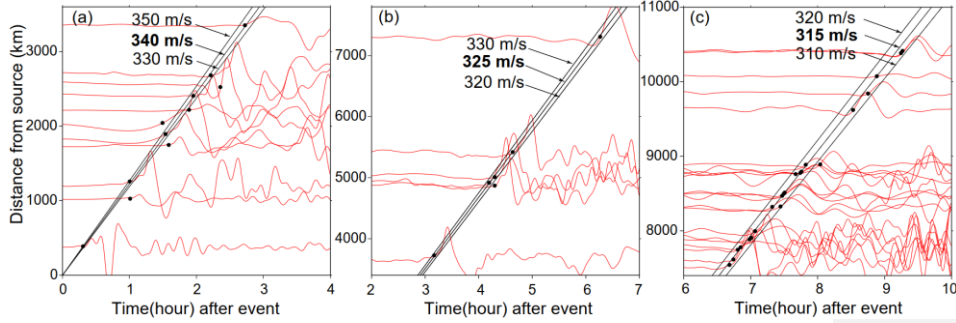
171 time, we analyze the waveforms recorded by the DART buoys in the Pacific Ocean. DART buoy with
172 pressure sensor deployed at the ocean's bottom records the sea level change that is transferred from
173 pressure records in Pascals, instead of direct water height. For the 2022 HTHH tsunami event, the
174 pressure fluctuation at DART buoy is a superposition of the pressure changes caused by tsunami and the
175 Lamb wave (Kubota et al., 2022). The Pacific DART buoys recorded the most discernible air-sea
176 coupling pulse in deep ocean with Lamb waves that arrived earlier than the theoretical tsunamis (Figure
177 1). The tsunami waveforms recorded by tide gauges did not clearly detect the tsunami signals associated
178 with the Lamb waves, therefore are not sufficient for further analysis (Figure 2). Thus, we estimate the
179 speed of Lamb waves using the waveforms recorded by the Pacific DART buoys. The Lamb wave
180 arrivals are limited within arrival time range from possible velocities of 280–340 m/s. The time points at
181 which the tsunami amplitudes first exceed 1 e-4 m above sea level are defined as Lamb wave arrivals.

182 Using different velocity values as constraints By carefully fitting the arrivals with different constant
183 velocities, we illustrate the velocities of Lamb wave were generally uniform, but slightly decrease with
184 the increase of propagation distance (Figure 3). The Lamb waves initially propagated radially at speed
185 of ~340 m/s before slowing to ~325 m/s after reaching ~3400 km, and further decreasing to ~315 m/s at
186 7400 km. In an isothermal troposphere assumption, the phase velocity of the Lamb wave (C_L) can be
187 estimated with the following equation (Gossard and Hooke, 1975b):

$$188 C_L = \sqrt{\frac{\gamma R T}{M}} \quad (2)$$

189 Where $\gamma = 1.4$ (air specific heat ratio corresponding to atmospheric temperature), $R = 8314.36 \text{ J kmol}^{-1} \text{ K}^{-1}$ (the universal gas constant), $M = 28.966 \text{ kg kmol}^{-1}$ (molecular mass for dry air) are constant for the
190 air, T is the absolute temperature in kelvin. Thus, Lamb wave velocity is mainly affected by the air
191 temperature, meaning the travelling velocity of lamb waves might decrease when propagating from
192 regions with high temperature towards those with low temperatures, e.g., the north pole. By assuming a
193 set of possible temperatures in January (Table 1), we calculated the velocities C_L could range between
194 312–343 m/s when temperatures vary between -30–20 °C. Therefore, the decreased velocity of the Lamb
195 waves could be a consequence of cooling of the air temperature.

带格式的: 字体: (默认) Times New Roman, 10 磅, 字体颜色: 文字 1, 图案: 清除 (自定义颜色(RGB(247,247,247)))



197
198 **Figure 3. Identifying the Lamb wave-induced tsunami velocities using different constant velocities**
199 **as constraints**
200 **Fitting the arrival times of normalized Lamb-induced tsunami waveforms with**
201 **different velocities.** Black dots mark the arrival times of the Lamb waves. Black lines represent

带格式的: 字体: (默认) Times New Roman, 10 磅, 加粗, 字体颜色: 文字 1

202 **Table 1. Estimated Lamb wave velocities in an isothermal troposphere assumption**

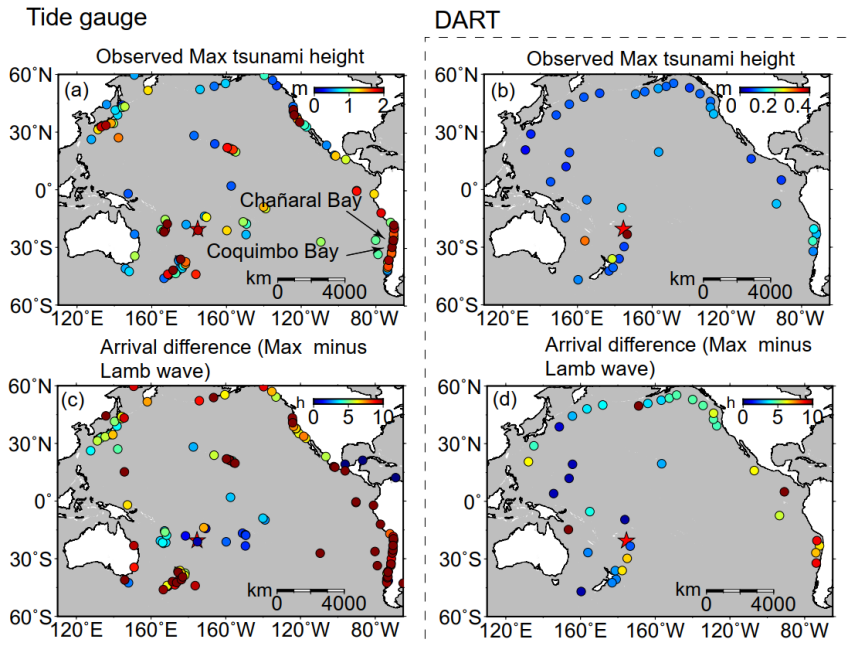
Celsius temperature (°C)	thermodynamic temperature (K)	C_L (m/s)
20	293.15	343.14
10	283.15	337.23
0	273.15	331.21
-10	263.15	325.19
-20	253.15	318.86
-30	243.15	312.49

203 **3.2 Tsunami features observed by DART buoys and Tide gauges**

204 The statistics of tsunami heights and arrival times recorded at 38 DART buoys and 116 tide gauges across
205 the Pacific Ocean are used to interpret the tsunami characteristics. The comparison of the statistical
206 characters between DART and tide gauge observations yields some useful information of the
207 hydrodynamic process of tsunami propagation and help identify tsunami wave components with different
208 traveling velocities.

209 The average value of the maximum tsunami wave height (trough-to-crest) for the 116 tide gauge stations
210 is ~1.2 m. Figure 4a shows tide gauges with large tsunami heights exceeding 2 m are mainly distributed
211 in coastlines with complex geometries (Figure S1a), such as gauges at New Zealand, Japan, and north
212 and south America. For example, the largest tsunami height among tide gauges is 3.6 m at a bay-shaped
213 coastal area Chañaral in Chile (Figure S1b). In sharp contrast to tide gauges, the maximum tsunami
214 heights of most Pacific DART buoys are less than 0.2 m. The largest tsunami height in the DART buoys
215 is only ~0.4 m recorded at the nearest one, 375 km from the volcano (Figure 4b). The comparison between

216 DART buoys and tide gauges indicate that the direct contribution of air-sea coupling to the tsunami
217 heights is probably in the level of tens of centimeters (Kubota et al., 2022). The meter-scale tsunami
218 heights at the coastlines suggest the bathymetric effect could play a major role during tsunami
219 propagation. In respect to the arrival of maximum tsunami waves, the time lags between Lamb waves
220 and the maximum heights of tide gauges mainly range between ~0–10 h (Figure 4c). The delayed times
221 of ~10 h are observed in New Zealand, Hawaii, and west coast of America (Figure 4c), suggesting the
222 interaction between tsunami waves and local topography/bathymetry delays the arrival of the maximum
223 waves (e.g., Hu et al., 2022). For example, the delayed maximum tsunami height can be attributed to the
224 edge waves (Satake et al., 2020) and resonance effect (Wang et al., 2021) from tsunami interplays with
225 bays/harbors, islands, and continental shelves of various sizes. The significant regional dependence of
226 the coastal tsunami heights and the time lags of the maximum tsunami waves can be attributed to the
227 complexity of local bathymetry, such as continental shelves with different slopes, and harbor/bay with
228 different shapes and sizes (Satake et al., 2020). On the other hand, for tsunami events with earthquake
229 origins (e.g. Heidarzadeh and Satake, 2013), the first waves recorded by DART buoys are normally
230 observed as the largest wave since DART buoys are located in the deep sea and less influenced by
231 bathymetric variation. In the case of Tonga tsunami event, we observe the inconsistency between the
232 arrivals of the Lamb wave-induced tsunami waves and the maximum tsunami heights (Figure 4d). The
233 time lags of the maximum waves of DART buoys present a coarsely increasing tendency with the
234 increasing distance from the volcano, which indicates the contribution of other tsunami generation
235 mechanism propagating with a uniform but lower speed than Lamb wave.



236
237 **Figure 4. The spatiotemporal signatures of the 2022 HTHH tsunami across the Pacific Ocean.** (a)
238 Observed the maximum tsunami height (trough-to-crest height) of tide gauges. (c) Arrival
239 differences between the maximum tsunami height of tide gauges and Lamb waves. (b) and (d) are
240 the same as (a) and (c) but for DART buoys.

241 **3.3 Tsunami components identified from wavelet analysis**

242 The statistical analysis of tsunami waveforms at tide gauges and DART buoys suggest the tsunami waves
243 likely contain several components with different source origins. To further identify these tsunami
244 components, we conduct wavelet analysis for tsunami waveforms recorded by representative DART
245 buoys and air pressure waveforms recorded by selected barometers. We demonstrate the analysis result
246 through the frequency-time (f-t) plot of wavelet which shows how energy and period vary at frequency
247 and time bands (Figure 5 and Figure 6). Tsunami components have clear signatures in all f-t plots as the
248 energy levels are quite large when they arrive. Figure 5 shows the wavelet analysis of six DART buoys
249 located in the vicinity of the eruption site (<3664 km). Figure 6 show the wavelet analysis of ten DART
250 buoys located in the Pacific rim which are far away from the source location. We observe three interesting
251 phenomena: 1) most of the tsunami wave energy is concentrated in four major period bands, i.e., 3–5
252 min, ~10–30 min, ~30–40 min, and ~80–100 min; 2) The significant tsunami component with period

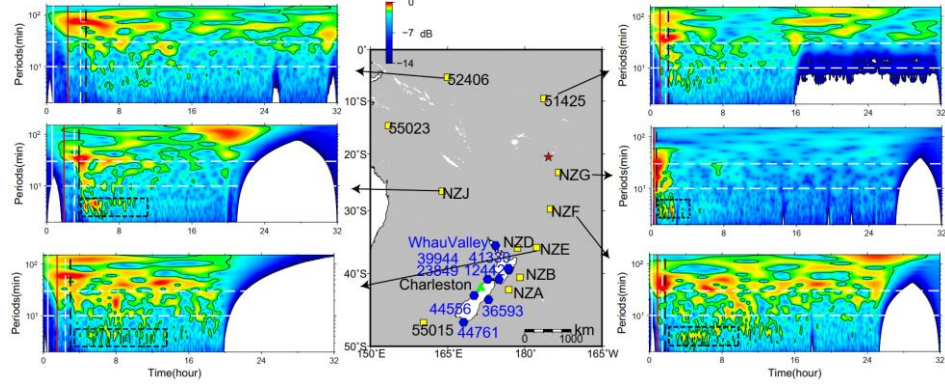
253 band of 3-5 mins are recorded by stations between the eruption site and the north tip of the New Zealand;
254 3) There exists one exceptional tsunami component with longer wave period of ~80–100 min mainly
255 recorded in the Tonga, the New Zealand and Hawaii, which travels even faster than the Lamb waves.
256 To further explore the source mechanism of these tsunami components, we take advantage of the
257 published information related to different propagating velocities of atmospheric gravity waves (Kubota
258 et al., 2022) and add four kinds of propagating velocities as criteria to differentiate the tsunami arrivals
259 from different sources (Figure 5 and Figure 6). The first reference speed is 1000 m/s related to the
260 radically propagating atmospheric shock waves near the source region (Matoza et al., 2022; Themens et
261 al., 2022). The second one is the velocities of Lamb wave ranging between 315–340 m/s derived from
262 the aforementioned analysis in section 3.1 (Figure 3). The third one is 200 m/s corresponding to the lower
263 limit of atmospheric gravity wave modes other than Lamb waves which were also excited by the volcanic
264 eruptions (Kubota et al., 2022). The last is the arrival time of conventional tsunami given by tsunami
265 modelling (Figure 1). The theoretical velocity of conventional tsunami is significantly nonuniform
266 spatially as compared with those of the atmospheric waves. The conventional tsunami propagation speed
267 is determined by the water depth along the propagation route. The velocity of non-dispersion shallow-
268 water waves (C_H) in the ocean is given by:

$$269 \quad C_H = \sqrt{g \cdot H} \quad (3)$$

270 Where g is gravity acceleration (9.81 m/s^2), H is the water depth. The propagation velocities of tsunami
271 are ~296–328 m/s in the deepest trenches on earth (i.e., ~11 km in Mariana Trench and ~9 km in Tonga
272 Trench). The velocities decrease quickly to only ~44 m/s at ~200 m depth along the edge of continental
273 shelf. With the average depth of ~4–5 km, the average velocities in the Pacific Ocean range between
274 ~200–224 m/s. Thus, theoretical tsunami velocities present significant slowness and variability. We
275 delineate the arrival times of the four reference speeds in Figures 5 and 6.

276 One particularly remarkable phenomenon is that the wave component with period of ~80–100 min
277 propagated at a very fast speed of ~1000 m/s in the vicinity of the HTTH site, i.e., New Zealand and
278 Hawaii (e.g., stations 52406, NZJ, NZE, 51425 in Figure 5, and 51407 in Fig. 6). We infer that the
279 tsunami component within ~80–100 min period band was likely produced by the atmospheric shock
280 waves during the initial stage of the volcanic eruption and spatially only cover the near-source region.
281 To verify this observation, we select 16 representative barometers located in the near-source region and

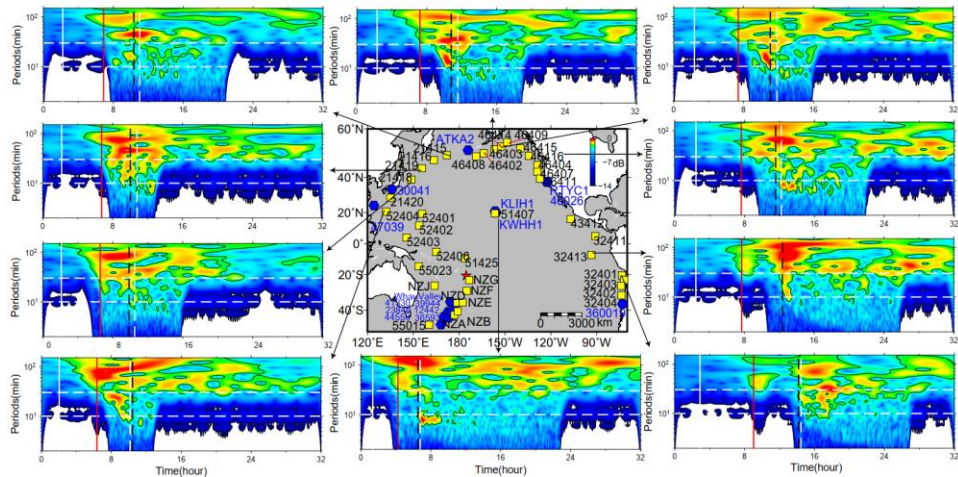
282 far-field area for wavelet analysis (see the locations in Figure 5 and Figure 6). Figure 7 shows the
283 waveforms of atmospheric pressure at selected locations and Figure 8 provides the frequency-time (f-t)
284 plot of wavelet analysis of some representative barometers. Interestingly, we are able to discern the air
285 pressure pulses prior to Lamb waves at barometers in New Zealand (the two columns on the left in Figure
286 7), although such signals are not detectable in waveforms recorded by barometers far from the source
287 (the two columns on the right in Figure 7). The spatial distribution of such unusual pressure changes
288 suggest that the fast travelling shock waves were only limited in the near-source region, as reflected in
289 the travelling ionospheric disturbances (Matoza et al., 2022; Themens et al., 2022). Additionally, we also
290 see that the long period signals of ~80–100 min appear in DART buoys far away from the eruption site.
291 Such signals may be related with the long-period gravity waves (Matoza et al., 2022).
292 The tsunami components at period band of ~30–40 min can be readily associated with Lamb waves
293 because the arrival times of the tsunami waves and Lamb waves have excellent match, as shown in the
294 tsunami data recorded by DART buoys (e.g., NZJ and 51425 in Figure 5; 51407, 32401 and 32413 in
295 Figure 6) and pressure data by barometers (Figure 8).
296 For the tsunami components with the period band of ~10–30 min, although the arrivals of ~10–30 min
297 tsunami components cover some theoretical tsunami arrival times, they do not consistently match. The
298 tsunami components occurring within the time period between Lamb waves and the lower gravity waves'
299 velocities has a good agreement with the velocity range of several atmospheric gravity wave modes
300 (Matoza et al., 2022; Themens et al., 2022; Kubota et al., 2022). Similarly, the air pressure data also show
301 energy peaks at ~10–30 min period band, which is consistent with the tsunami data (Figure 8). Such
302 consistency further verifies the contribution of atmospheric gravity waves to the volcanic tsunami.
303 The tsunami components with the shortest period of ~3–5 min (stations NZE, NZF, NZG and NZJ;
304 marked with black dashed squares in Figure 5) are only observed at DART records near the eruption
305 location. Meanwhile, the arrival times of these components agree well with the modelled arrivals of
306 conventional tsunami. Thus, we believe the observed shortest period band should originate from the
307 seafloor crustal deformation. We further infer that this component could be generated by the partial
308 underwater caldera collapse and/or subaerial/submarine landslide failures associated with 2022 HTHH
309 volcanic eruption.



310

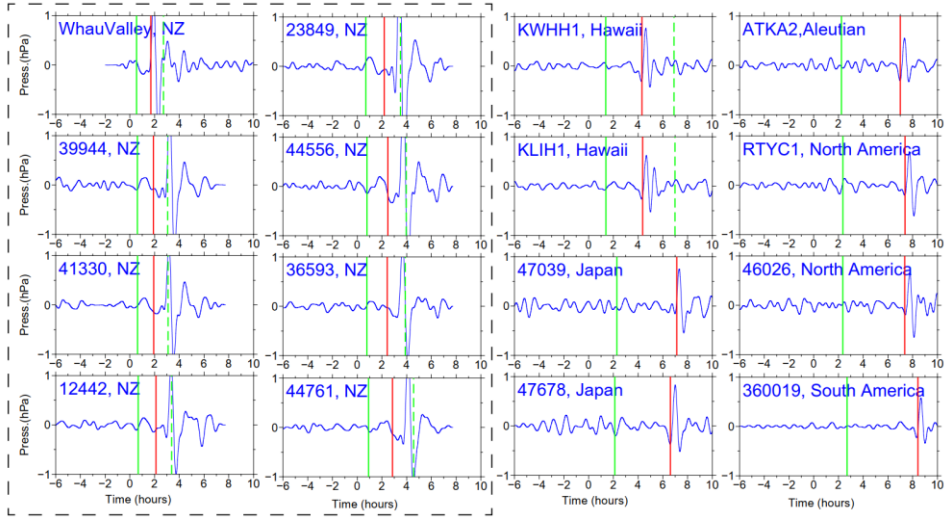
311 Figure 5. Wavelet analysis of representative DART buoys in the vicinity of the HTHH volcano. In
 312 each sub-plot, the solid vertical white lines mark the arrival time with travelling velocity of 1000
 313 m/s. The solid vertical red lines mark the arrivals of Lamb waves. The dashed vertical white lines
 314 mark lower limit of AGWs' velocity of 200 m/s (Kubota et al., 2022). The dashed vertical black
 315 lines represent the theoretical tsunami arrivals. The dashed horizontal white lines mark two
 316 reference wave periods of 10 min and 30 min. The blue hexagons represent the locations of
 317 barometers. Green triangle makes the location of the tide gauges at Charleston. Decibel (dB) is
 318 calculated from: $dB = 10 \log(A/A_0)$, where A is wavelet power, A_0 is a reference wavelet power of
 319 the maximum one (Thomson and Emery, 2014).

320



321

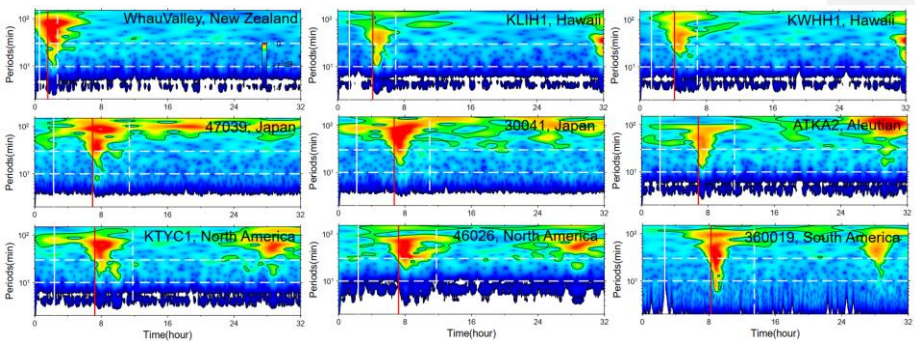
322 **Figure 6.** Wavelet analysis of representative DART buoys far away from the HTHH volcano. In
 323 each sub-plot, the solid vertical white lines mark the arrival time with travelling velocity of 1000
 324 m/s. The solid vertical red lines mark the arrivals of Lamb waves. The dashed vertical white lines
 325 mark lower limit of AGWs' velocity of 200 m/s. The dashed vertical black lines represent the
 326 theoretical tsunami arrivals. The dashed horizontal white lines mark two reference wave periods
 327 of 10 min and 30 min. The blue hexagons represent the locations of barometers.



328

329 **Figure 7.** Shockwave-related atmospheric pressure waveforms of selected barometers in the Pacific
 330 Ocean. All traces have been filtered between 30 min and 150 min. In each sub-plot, the solid vertical
 331 green lines mark the arrival time with travelling velocity of 1000 m/s. The solid vertical red lines
 332 mark the arrivals of Lamb waves. The dashed vertical green lines mark lower limit of AGWs'
 333 velocity of 200 m/s.

334



335

336 **Figure 8.** Wavelet analysis of some representative barometers. In each sub-plot, the solid vertical
 337 white lines mark the arrival time with travelling velocity of 1000 m/s. The solid vertical red lines
 338 mark the arrivals of Lamb waves. The dashed vertical white lines mark lower limit of AGWs'
 339 velocity 200 m/s. The dashed horizontal white lines mark three reference periods of 10 min and 30
 340 min.

341 **4. Discussion**

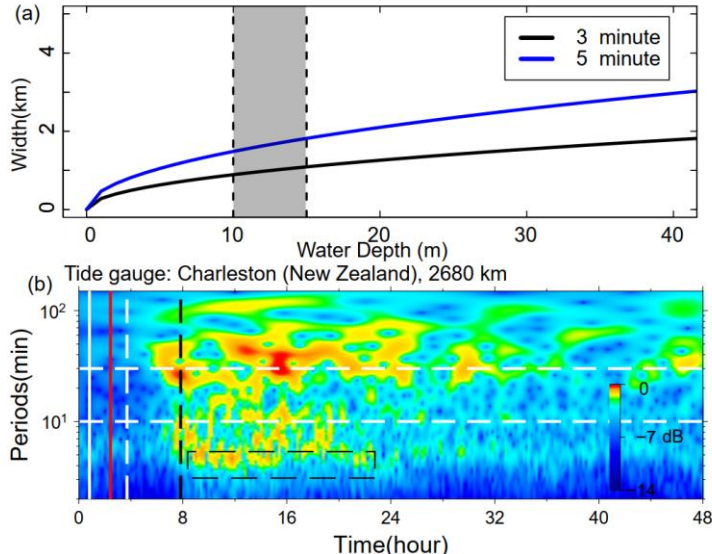
342 **4.1 Tsunami from Caldera Collapse and Its Long-distance Traveling Capability**

343 The tsunami wave energy distributed in different period bands is identified with reference arrival times.
344 The tsunami component with 3–5 min period is most likely generated by seafloor crustal deformation in
345 the volcanic site, but specific mechanism is not determined. A variety of possible scenarios associated
346 with the eruption could be responsible for the near-field tsunami waves, such as volcanic earthquakes,
347 pyroclastic flows entering the sea, underwater caldera flank collapse, and subaerial/submarine failures
348 (Self and Rampino, 1981; Pelinovsky et al., 2005). To further investigate the source mechanism, we
349 apply a simplified model (Rabinovich, 1997) to estimate the probable dimension of tsunami source:

$$350 L = \frac{T\sqrt{gH}}{2} \quad (4)$$

351 Where L is the typical dimension (length or width) of the tsunami source, H is average water depth in the
352 source area, g is the gravity acceleration, and T is primary tsunami period. By comparing with the post-
353 2015 morphology of the HTHH caldera which was obtained through drone photogrammetry and
354 multibeam sounder surveys, Stern et al. (2022) estimate that much of the newly-formed Hunga Tonga
355 Island and the 2014/2015 cone were destroyed by the 2022 eruption, and the vertical deformation of
356 Hunga Ha'apai Island is ~10–15 m (Stern et al., 2022). With no more quantitative constraint of the
357 seafloor deformation, we tentatively assume H as 10–15 m, then the possible dimension of seafloor
358 crustal deformation responsible for the small-scale tsunami could be in the scale of 0.8–1.8 km (Figure
359 9a). The estimated size is very likely from partial caldera collapse that usually has limited scale in
360 volcanic site (Ramalho et al., 2015; Omira et al., 2022). If it is the case, the partial flank collapse could
361 be located between Hunga Tonga and Hunga Ha'apai Islands.

362



363
 364 **Figure 9. Mechanism of tsunami component with 3–5 min period.** (a) The source dimension
 365 estimated by equation 4. (b) Wavelet analysis of tide gauge at Charleston, New Zealand, 2680 km
 366 away from the eruption site. The solid vertical white line marks the arrival time with travelling
 367 velocity of 1000 m/s. The solid vertical red line marks the arrival of Lamb wave. The dashed
 368 vertical white line marks lower limit of AGWs' velocity 200 m/s. The dashed vertical black line
 369 marks the theoretical tsunami arrivals.

370 An interesting phenomenon is that the tsunami component with 3–5 min period can still be observed in
 371 a bay-shaped coastal area at Charleston in New Zealand (see the location in Figure 5) which is 2680 km
 372 away from the eruption site and maintains a high energy level lasting up to 14 h (Figure 9b). The long-
 373 traveling capability could be associated with the ~10000 m deep water depth of the Tonga Trench that
 374 keeps the source signals from substantial attenuation. In deep open ocean, the wavelength of a tsunami
 375 can reach two hundred kilometers, but the height of the tsunami may be only a few centimeters. Tsunami
 376 waves in the deep ocean can travel thousands of kilometers at high speeds, meanwhile losing very little
 377 energy in the process. The long oscillation can be attributed to the multiple reflections of the incoming
 378 waves trapped in the shallow-water bay at Charleston.

379 Generally, devastating tsunamis with long-distance travelling capability are mostly generated by
 380 megathrust earthquakes (Titov et al., 2005). Caldera collapses or submarine landslides with limited scale
 381 normally only generate local tsunamis, e.g., the 1998 PNG (Papua New Guinea) tsunami event (Kawata
 382 et al., 1999) and the 1930 Cabo Girão tsunami event (Ramalho et al., 2015). Therefore, it's exceptional

383 that the tsunami component from scale-limited failure could travel at-least 2680 km away from the
384 eruption site. It demonstrates that tsunamis from small-scale tsunamigenic source have the capability to
385 travel long distance and cause long oscillation at favored condition, e.g., deep trench, ocean ridge and
386 bay-shaped coasts.

387 **4.2 The Possible Mechanisms of Long Tsunami Oscillation**

388 An important tsunami behavior of the 2022 HTHH tsunami is the long-lasting oscillation ~ 3 days in the
389 Pacific Ocean (Figure 10a), which is comparable to that of the 2011 Tohoku tsunami, ~4 days
390 (Heidarzadeh and Satake, 2013). We demonstrate the duration time of the tsunami oscillation through
391 ARMS (Averaged-Root-Mean-Square) approach that is a measure of absolute average tsunami amplitude
392 in a time period. The long-lasting tsunami energy can be observed at many regions, such as the coasts of
393 New Zealand, Japan, Aleutian, Chile, Hawaii, and west coasts of America. Several mechanisms could
394 account for the long-lasting tsunami, including (1) Lamb waves circling the Earth multiple times
395 (Amores et al., 2022; Matoza et al., 2022), (2) resonance effect between ocean waves and atmospheric
396 waves (Kubota et al., 2022), and (3) bathymetric effect. We discuss the contribution of each mechanism
397 in the following section.

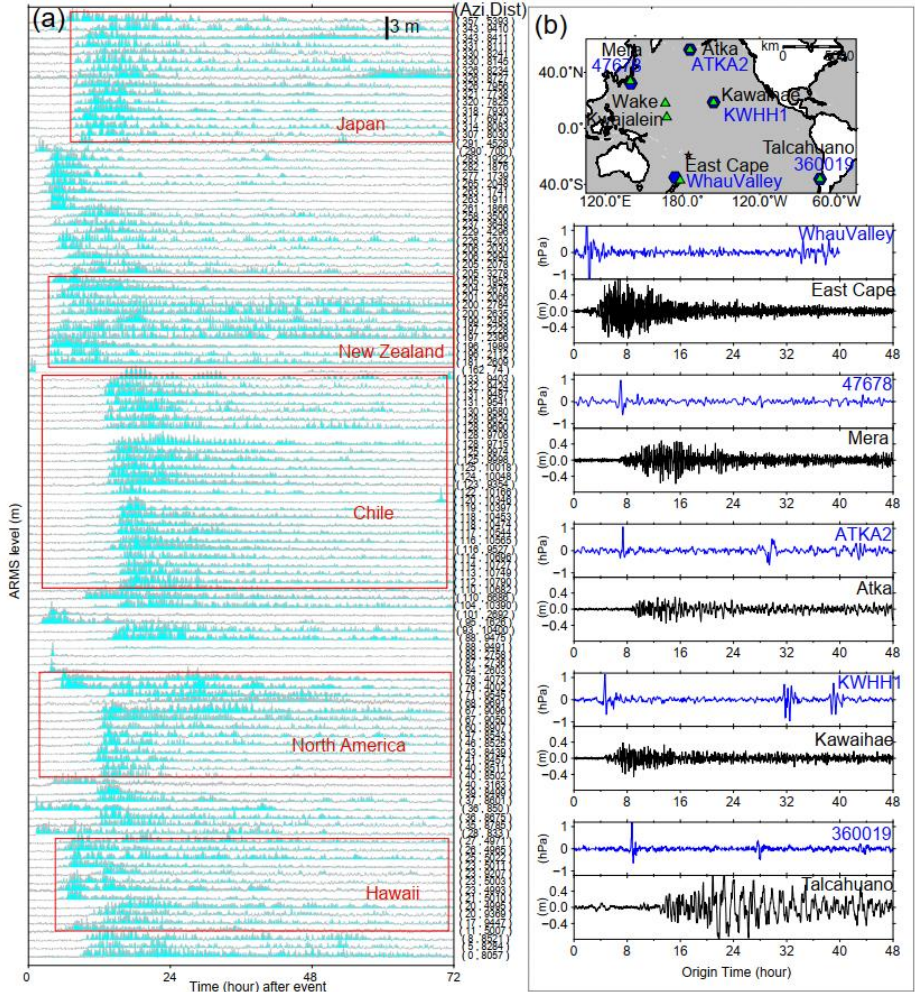
398 To investigate the contribution of Lamb wave to the long-lasting tsunami, we compare the air pressure
399 disturbances recorded by selected barometers together with the tsunami waveforms of nearby tide gauges
400 (Figure 10b). While the barometers present discernible wave pulses at each Lamb wave's arrival, only
401 the first Lamb wave triggered clear tsunami signal and no detectable tsunami signatures correspond to
402 the following passage, suggesting the Lamb waves do not directly contribute to the long oscillation.

403 The resonance effects between ocean waves and atmospheric waves could contribute to the long
404 oscillation on coastlines. Besides the Lamb wave, Watanabe et al., 2022 detected internal Pekeris wave
405 which propagate with a slower horizontal phase speed of ~245 m/s and gravity waves with even slower
406 propagation speed by analyzing radiance observations taken from the Himawari-8 geostationary satellite.
407 Atmospheric waves with such speeds are more likely to resonant with the conventional tsunami waves
408 and provide continuous energy supply (Kubota et al., 2022).

409 To examine the role of local bathymetry in the long-lasting tsunami, we choose a well-studied and well-
410 recorded event: the 2011 Mw 9.0 Tohoku tsunami as a reference event and compare the tsunami records
411 of these two events at the same coastal stations. Although the two tsunami events were generated by

412 completely different mechanisms, i.e., large-scale seafloor deformation for the Mw 9.0 megathrust
413 earthquake (Mori et al., 2011) and fast-moving atmospheric waves for the Mw 5.8 volcanic eruption
414 (Matoza et al., 2022), they both produced widespread transoceanic tsunamis which were well recorded
415 in the Pacific DART buoys and tide gauges. In the near-field, the 2011 Tohoku earthquake produced
416 runup up to 40 m at Miyako in the Iwate Prefecture in Japan's Tohoku region (Mori et al., 2011). The
417 epicenter is approximately 70 km east coast of the Oshika Peninsula of Tohoku region. However, the
418 2022 HTHH tsunami produced only ~13 m runup in the near field from eyewitness accounts in
419 Kanokupolu, 60 km from the volcano (Lynett et al., 2022). However, in the far-field (>1000 km), we
420 observe comparable tsunami wave heights in certain coastal regions. Based on the tsunami records at 21
421 tide gauges surrounding the Pacific Ocean, Heidarzadeh & Satake (2013) calculated the average value
422 of the maximum tsunami heights (trough-to-crest) of the 2011 Tohoku tsunami is 1.6 m with the largest
423 height of 3.9 m at the Coquimbo Bay in Chile (Heidarzadeh and Satake, 2013). Coincidentally, the statistics
424 of 116 tide gauges in this study also suggest the average tsunami heights of the 2022 HTHH tsunami is
425 around the same order, ~1.2 m, among which, the largest height is 3.6 m at Chañaral Bay in Chile.
426 Interestingly, in the coastal region of South America, the locations of the largest tsunami heights of both
427 events are adjacent (Figure 4a), i.e., Coquimbo (the 2011 Tohoku) and Chañaral (The 2022 HTHH).
428 To further compare the far-field hydrodynamic processes between these two events quantitatively, we
429 conduct wavelet analysis for four representative tide gauges distributed across the Pacific Ocean, i.e.
430 coastal gauges at East Cape in New Zealand, Kwajalein Island, Wake Island, and Talcahuano in Chile
431 (see their locations in Figures 10b). The temporal changes of tsunami energy of both events can be seen
432 in Figure 11. At each tide gauge, the tsunami energy of the 2011 HTHH (Figure 11a) and the 2022 Tohoku
433 tsunamis (Figure 11b) for the first few hours after the arrivals is nonuniform with different significant
434 peaks distributed within a wide period band of ~3–100 min. Then, the following long-lasting energy of
435 the both at each station presents similar pattern and is concentrated at identical and fairly narrower period
436 channel, i.e., ~20–30 min at East Cape in New Zealand, ~40–60 min at Kwajalein Island, ~10 min at
437 Wake Island, and ~100 min at Talcahuano in Chile, which reflects the local bathymetric effects of natural
438 permanent oscillations (Hu et al., 2022; Satake et al., 2020). Specifically, many bathymetric effects can
439 contribute to the long-lasting tsunami, such as multiple reflections across the basins, or the continental
440 shelves, and the excited tsunami resonance in bays/harbors with variable shapes and sizes (Aranguiz et

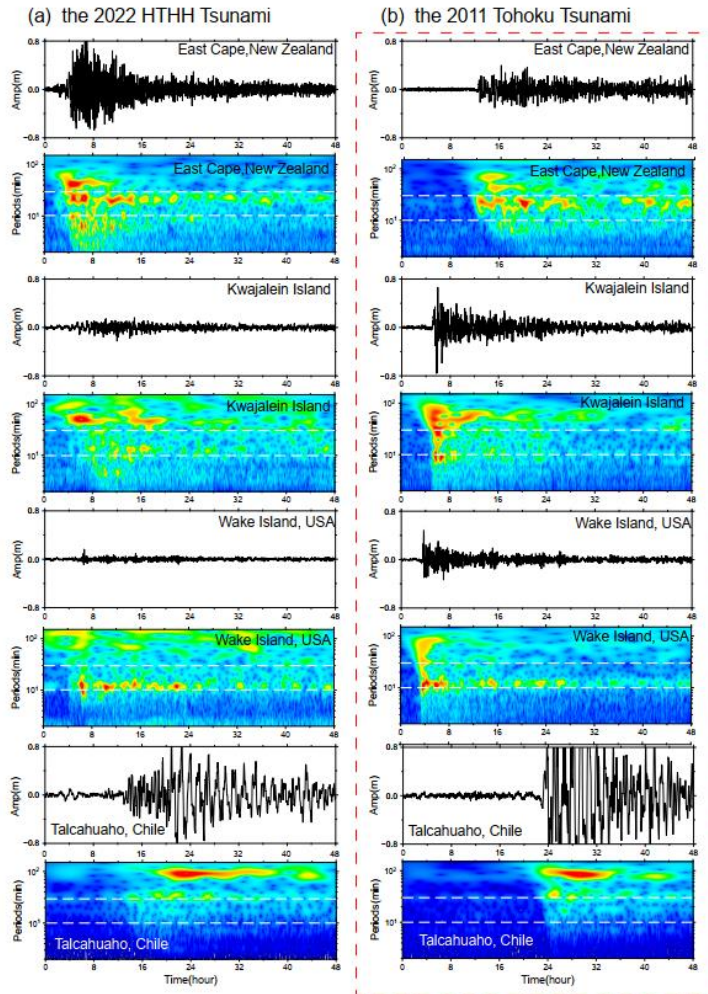
441 al., 2019; Satake et al., 2020). For example, tide gauges around New Zealand are primarily distributed in
442 harbors/ports with major natural oscillation modes of ~20–30 min (De Lange and Healy, 1986; Lynett et
443 al., 2022). The first oscillation mode of central Chile is centered around ~100 min (Aranguiz et al., 2019).
444 Consequently, Figure 11 illustrates that the long-lasting tsunami energy of the two events is respectively
445 distributed in 20–30 min period at East Cape in New Zealand and in ~100 min period at Talcahuano in
446 central Chile. The coupling of bathymetric oscillation mode with tsunami containing similar-period wave
447 results in the excitement of tsunami resonance, which amplifies tsunami waves and prolongs the tsunami
448 oscillation at the two stations (Heidarzadeh et al., 2019, 2021; Hu et al., 2022; Wang et al., 2022).
449 Simply put, we do not have clear evidence that atmospheric acoustic-gravity waves from the 2022 HTHH
450 eruption directly contribute to the long-lasting tsunami, but the resonance effect associated with ocean
451 waves could a possible source of increased wave energy and amplification. However, the similarity of
452 far-field hydrodynamic behaviors between the 2022 HTHH volcanic tsunami and the 2011 Tohoku
453 seismogenic tsunami well demonstrates the both went through similar hydrodynamic processes after their
454 arrivals. The consistency favors that the long-lasting tsunami of 2022 HTHH tsunami event can very
455 likely be attributed by the interplays between local bathymetry and conventional tsunami left after each
456 passage of atmospheric waves, which can well explain why the two completely distinct tsunami events
457 possess a comparable duration time.



458

459 **Figure 10. Tsunami duration.** (a) Tsunami durations at Pacific 116 tide gauges through ARMS level
 460 approach. (b) the location of barographs (blue curves) and nearby tide gauges (green curves), as
 461 well as their waveforms.

462
 463



464
465
466
467

Figure 11. Wavelet analysis of tsunami waveforms recorded by 4 tide gauges during (a) the 2022 HTHH tsunami event, and (b) the 2011 Tohoku tsunami event. Horizontal white dashed lines respectively mark reference periods of 10 min and 30 min.

468 **4.3 Challenges for Tsunami Warning**

469 The generation mechanisms and hydrodynamic characteristics of the 2022 HTHH volcanic tsunami are
470 more complicated than pure seismogenic tsunami, which challenge the traditional tsunami warning
471 approach.

472 The first challenge is posed by the tsunami components with propagating velocities faster than the

473 conventional tsunami. The Tonga volcanic tsunami event provides an excellent example which highlights
474 that the tsunamigenic mechanisms are not limited to tectonic activities related with the sudden seafloor
475 displacements, but also include a variety of atmospheric waves with distinct propagation velocities. The
476 tsunami components in 2022 HTHH event generated by the air-sea coupling possess a wide range of
477 velocities from 1000 m/s to 200 m/s. The Lamb waves recorded in both the 2022 HTHH event and the
478 1833 Krakatoa volcanic event traveled along the Earth's surface globally for several times (Carvajal et
479 al., 2022). The tsunami waves produced by Lamb waves, the wave components associated with resonance
480 of the air-sea coupling and their superimposition increase the difficulty of tsunami warning.
481 Another critical challenge is associated with the interplays between tsunami waves and local bathymetry.
482 The tsunami waves left by each passage of the atmospheric waves can interact with local bathymetry at
483 coastlines, such as continental shelves with different slopes, and harbor/bay with different shapes and
484 sizes. The interaction can intensify the tsunami impact and excite a variety of natural oscillation periods.
485 The 2022 HTHH tsunami with an extremely wide period range of ~2–100 min have a great potential to
486 couple with the excited natural oscillations and form extensive tsunami resonance phenomena. The
487 resonance effects result in long-lasting oscillation and delayed tsunami wave peaks. The uncertain
488 arrivals of the maximum tsunami waves pose an extra challenge to tsunami warning.

4895. Conclusion

490 In the study, we explore the tsunamigenic mechanisms and the hydrodynamic characteristics of the 2022
491 HTHH volcanic tsunami event. Through extensive analysis of waveforms recorded by the DART buoys,
492 tide gauges and barometers in the Pacific Ocean, we reach the main findings as follows:
493 (1) We identify four distinct tsunami wave components based on their distinct propagation velocities or
494 period bands (~80–100 min, 10–30 min, 30–40 min, and 3–5 min). The generation mechanisms of these
495 tsunami components range from air-sea coupling to seafloor crustal deformation during the volcanic
496 eruption.
497 (2) The first-arriving tsunami component with 80–100 min period was most likely from shock wave
498 spreading at a velocity of ~1000 m/s in the vicinity of the eruption. This tsunami component was not
499 clearly identified by currently available publication and it's not easy to be visually observed through time
500 series of the waveforms. The physical mechanism is yet to be understood. The second tsunami component

501 with 30–40 min period was from Lamb waves, and was the most discussed tsunami source of this event
502 so far. A thorough analysis of DART measurements indicates that the Lamb waves traveled at the speed
503 of ~340 m/s in the vicinity of the eruption and decreased to ~315 m/s when traveling away due to cooling
504 of the air temperature. The third tsunami component was from some atmospheric gravity wave modes
505 with propagation velocity faster than 200 m/s but slower than Lamb waves. The last tsunami component
506 with the shortest periods 3–5 min was probably produced by partial caldera collapse with estimated
507 dimension of ~0.8–1.8 km.

508 (3) Although the resonance effect with the atmospheric acoustic-gravity waves could be a source of
509 increased wave energy, its direct contribution to the long-lasting oscillation is not demonstrated yet.
510 However, the comparison of hydrodynamical characteristics between the 2022 HTHH tsunami event and
511 the 2011 Tohoku tsunami event well demonstrated that the interactions between the ocean waves left by
512 atmospheric waves and local bathymetry contribute to the long-lasting Pacific oscillation of the 2022
513 tsunami event.

514 (4) The extraordinary features of this rare volcanic tsunami event challenge the current tsunami warning
515 system which is mainly designed for seismogenic tsunamis. It is necessary to improve the awareness of
516 people at risks about the potential tsunami hazards associated with volcanic eruptions. New approaches
517 are expected to be developed for tsunami hazard assessments with these unusual sources: various
518 atmospheric waves radiated by volcanic eruptions besides those traditionally recognized, e.g.
519 earthquakes, landslides, caldera collapses and pyroclastic flows etc.

520 **Acknowledgment**

521 This work was supported by National Natural Science Foundation (No 41976197, No 12002099),
522 Innovation Group Project of Southern Marine Science and Engineering Guangdong Laboratory (Zhuhai)
523 (No. 311021002), Key Research and Development Program of Hainan Province (No. ZDYF2020209),
524 Southern Marine Science and Engineering Guangdong Laboratory (Zhuhai) (SML2021SP305) and
525 Fundamental Research Funds for the Central Universities, Sun Yat-sen University (2021qntd23).
526 The JAGURS tsunami simulation code is employed for tsunami modelling (Baba et al., 2015;
527 <https://zenodo.org/record/6118212#.Yk98qdtBxPY>). Bathymetry data are obtained from GEBCO at
528 <http://www.gebco.net>. The sea level records in deep ocean are available from the Deep Ocean Assessment

529 and Reporting of Tsunamis (DART) buoy network in the Pacific (<https://nctr.pmel.noaa.gov/Dart/>), and
530 GeoNet New Zealand DART network (<https://tilde.geonet.org.nz>). The sea level records of tide gauges
531 are downloaded from UNESCO/ IOC (<http://www.ioc-sealevelmonitoring.org/>). Barometer data are
532 provided by the following providers: Dirección Meteorológica de Chile
533 (<https://climatologia.meteochile.gob.cl>), NOAA National Weather Service
534 (<https://www.weather.gov/ilm/observations>), Japan Meteorological Agency (<https://www.jma.go.jp>),
535 The UK Met Office Weather Observation (<https://www.metoffice.gov.uk/observations>), and Fiji
536 Meteorological Service (<https://www.met.gov.fj>).

537 **Reference**

538 Adam, D.: Tonga volcano created puzzling atmospheric ripples, *Nature*,
539 <https://doi.org/10.1038/d41586-022-00127-1>, 2022.

540 Amores, A., Monserrat, S., Marcos, M., Argüeso, D., Villalonga, J., Jordà, G., and Gomis, D.:
541 Numerical simulation of atmospheric Lamb waves generated by the 2022 Hunga-Tonga volcanic
542 eruption, *Geophys. Res. Lett.*, 49, e2022GL098240, <https://doi.org/10.1029/2022GL098240>, 2022.

543 Aranguiz, R., Catalán, P. A., Cecioni, C., Bellotti, G., Henríquez, P., and González, J.: Tsunami
544 Resonance and Spatial Pattern of Natural Oscillation Modes With Multiple Resonators, *J. Geophys.*
545 *Res. Ocean.*, 124, 7797–7816, <https://doi.org/10.1029/2019JC015206>, 2019.

546 Baba, T., Takahashi, N., Kaneda, Y., Ando, K., Matsuoka, D., and Kato, T.: Parallel Implementation of
547 Dispersive Tsunami Wave Modeling with a Nesting Algorithm for the 2011 Tohoku Tsunami, *Pure*
548 *Appl. Geophys.*, 172, 3455–3472, <https://doi.org/10.1007/s00024-015-1049-2>, 2015.

549 Bevis, M., Taylor, F. W., Schutz, B. E., Recy, J., Isacks, B. L., Helu, S., Singh, R., Kendrick, E.,
550 Stowell, J., Taylor, B., and Calmantli, S.: Geodetic observations of very rapid convergence and back-
551 arc extension at the tonga arc, *Nature*, 374, 249–251, <https://doi.org/10.1038/374249a0>, 1995.

552 Billen, M. I., Gurnis, M., and Simons, M.: Multiscale dynamics of the Tonga–Kermadec subduction
553 zone, *Geophys. J. Int.*, 153, 359–388, <https://doi.org/10.1046/j.1365-246X.2003.01915.x>, 2003, 2003.

554 Carvajal, M., Sepúlveda, I., Gubler, A., and Garreaud, R.: Worldwide Signature of the 2022 Tonga
555 Volcanic Tsunami, *Geophys. Res. Lett.*, 49, e2022GL098153, <https://doi.org/10.1029/2022GL098153>,
556 2022.

557 Duncombe, J.: The Surprising Reach of Tonga's Giant Atmospheric Waves.pdf, Eos (Washington.
558 DC), 103, <https://doi.org/10.1029/2022EO220050>, 2022.

559 Edmonds, M.: Hunga-Tonga-Hunga-Ha'apai in the south Pacific erupts violently, *Temblor*,
560 <https://doi.org/10.32858/temblor.231>, 2022.

561 Garvin, J. B., Slayback, D. A., Ferrini, V., Frawley, J., Giguere, C., Asrar, G. R., and Andersen, K.:
562 Monitoring and Modeling the Rapid Evolution of Earth's Newest Volcanic Island: Hunga Tonga
563 Hunga Ha'apai (Tonga) Using High Spatial Resolution Satellite Observations, *Geophys. Res. Lett.*, 45,
564 3445–3452, <https://doi.org/10.1002/2017GL076621>, 2018.

565 Gossard, E. E. and Hooke, W. H.: Waves in the Atmosphere: Atmospheric Infrasound and Gravity
566 Waves—Their Generation and Propagation, Elsevier, 1975a.

567 Gossard, E. E. and Hooke, W. H.: Waves in the Atmosphere, Amsterdam: Elsevier, 1975b.

568 Heidarzadeh, M. and Satake, K.: Waveform and Spectral Analyses of the 2011 Japan Tsunami Records
569 on Tide Gauge and DART Stations Across the Pacific Ocean, *Pure Appl. Geophys.*, 170, 1275–1293,
570 <https://doi.org/10.1007/s00024-012-0558-5>, 2013.

571 Heidarzadeh, M. and Satake, K.: Excitation of Basin-Wide Modes of the Pacific Ocean Following the
572 March 2011 Tohoku Tsunami, *Pure Appl. Geophys.*, 171, 3405–3419, <https://doi.org/10.1007/s00024-013-0731-5>, 2014.

573 Hu, G., Feng, W., Wang, Y., Li, L., He, X., Karakaş, Ç., and Tian, Y.: Source characteristics and
574 exacerbated tsunami hazard of the 2020 Mw 6.9 Samos earthquake in eastern Aegean Sea, *J. Geophys.
575 Res. Solid Earth*, 127, e2022JB023961, <https://doi.org/10.1029/2022JB023961>, 2022.

576 Kawata, Y., Benson, B. C., Borrero, J. C., Borrero, J. L., Davies, H. L., Lange, W. P. de, Imamura, F.,
577 Letz, H., Nott, J., and Synolakis, C. E.: Tsunami in Papua New Guinea Was as Intense as First
578 Thought, *Eos, Trans. Am. Geophys. Union*, 80, 9, <https://doi.org/10.1029/99EO00065>, 1999.

579 Kristeková, M., Kristek, J., Moczo, P., and Day, S. M.: Misfit Criteria for Quantitative Comparison of
580 Seismograms, *Bull. Seismol. Soc. Am.*, 96, 1836–1850, <https://doi.org/10.1785/0120060012>, 2006.

581 Kubota, T., Saito, T., and Nishida, K.: Global fast-traveling tsunamis by atmospheric pressure waves
582 on the 2022 Tonga eruption, *Science* (80-), <https://doi.org/10.1126/science.abo4364>, 2022.

583 Kulichkov, S. N., Chunchuzov, I. P., Popov, O. E., Gorchakov, G. I., Mishenin, A. A., Perepelkin, V.
584 G., Bush, G. A., Skorokhod, A. I., Yu. A. Vinogradov, Semutnikova, E. G., Šepic, J., Medvedev, I. P.,

586 Gushchin, R. A., Kopeikin, V. M., Belikov, I. B., Gubanova, D. P., and A. V. Karpov & A. V.
587 Tikhonov: Acoustic-Gravity Lamb Waves from the Eruption of the Hunga-Tonga-Hunga-Hapai
588 Volcano, Its Energy Release and Impact on Aerosol Concentrations and Tsunami, *Pure Appl.*
589 *Geophys.*, <https://doi.org/10.1007/s00024-022-03046-4>, 2022.
590 Lamb, H.: *Hydrodynamics*, Cambridge Univ. Press, 1932.
591 De Lange, W. P. and Healy, T. R.: New Zealand tsunamis 1840–1982, *New Zeal. J. Geol. Geophys.*,
592 29, 115–134, <https://doi.org/10.1080/00288306.1986.10427527>, 1986.
593 Lin, J., Rajesh, P. K., Lin, C. C. H., Chou, M., Liu, J.-Y., Yue, J., Hsiao, T.-Y., Tsai, H.-F., Chao, H.-
594 M., and Kung, M.-M.: Rapid Conjugate Appearance of the Giant Ionospheric Lamb Wave Signatures
595 in the Northern Hemisphere After Hunga- Tonga Volcano Eruptions, *Geophys. Res. Lett.*, 49,
596 e2022GL098222, <https://doi.org/10.1029/2022GL098222>, 2022.
597 Liu, P. L.-F. and Higuera, P.: Water waves generated by moving atmospheric pressure : Theoretical
598 analyses with applications to the 2022 Tonga event, *arXiv Prepr.*,
599 <https://doi.org/10.48550/arXiv.2205.05856>, 2022.
600 Liu, X., Xu, J., Yue, J., and Kogure, M.: Strong Gravity Waves Associated With Tonga Volcano
601 Eruption Revealed by SABER Observations, *Geophys. Res. Lett.*, 49, e2022GL098339,
602 <https://doi.org/10.1029/2022GL098339>, 2022.
603 Lynett, P., McCann, M., Zhou, Z., Renteria, W., Borrero, J., Greer, D., Fa'anunu, 'Ofa, Bosserelle, C.,
604 Jaffe, B., Selle, S. La, Ritchie, A., Snyder, A., Nasr, B., Bott, J., Graehl, N., Synolakis, C., Ebrahimi,
605 B., and Cinar, G. E.: Diverse tsunamigenesis triggered by the Hunga Tonga-Hunga Ha'apai eruption,
606 *Nature*, 609, 728–733, <https://doi.org/10.1038/s41586-022-05170-6>, 2022.
607 Matoza, R. S., Matoza, R. S., Fee, D., Assink, J. D., Iezzi, A. M., Green, D. N., Kim, K., Lecocq, T.,
608 Krishnamoorthy, S., Lalande, J., Nishida, K., and Gee, K. L.: Atmospheric waves and global
609 seismoacoustic observations of the January 2022 Hunga eruption ,Tonga, *Science* (80- .),
610 <https://doi.org/10.1126/science.abo7063>, 2022.
611 Mori, N., Takahashi, T., Yasuda, T., and Yanagisawa, H.: Survey of 2011 Tohoku earthquake tsunami
612 inundation and run-up, *Geophys. Res. Lett.*, 38, L00G14, <https://doi.org/10.1029/2011GL049210>,
613 2011.
614 NASA: National Aeronautics and Space Administration, "Dramatic changes at Hunga Tonga-Hunga

615 Ha'apai," 2022.

616 Nomanbhoy, N. and Satake, K.: Generation mechanism of tsunamis from the 1883 Krakatau Eruption,
617 *Geophys. Res. Lett.*, 22, 509–512, <https://doi.org/10.1029/94GL03219>, 1995.

618 Omira, R., Baptista, M. A., Quartau, R., Ramalho, R. S., Kim, J., Ramalho, I., and Rodrigues, A.: How
619 hazardous are tsunamis triggered by small-scale mass-wasting events on volcanic islands ? New
620 insights from Madeira–NE Atlantic, *Earth Planet. Sci. Lett.*, 578, 117333,
621 <https://doi.org/10.1016/j.epsl.2021.117333>, 2022.

622 Otsuka, S.: Visualizing Lamb Waves From a Volcanic Eruption Using Meteorological Satellite
623 Himawari-8, *Geophys. Res. Lett.*, 49, e2022GL098324, <https://doi.org/10.1029/2022GL098324>, 2022.

624 Pelinovsky, E., Choi, B. H., Stromkov, A., Didenkulova, I., and Kim, H.: Analysis of Tide-Gauge
625 Records of the 1883 Krakatau Tsunami. In: Satake, K. (eds) *Tsunamis, Adv. Nat. Technol. Hazards*
626 *Res.*, 23, Springer, Dordrech, https://doi.org/10.1007/1-4020-3331-1_4, 2005.

627 Le Pichon, A., Blanc, E., and Hauchecorne, A.: Infrasound monitoring for atmospheric studies,
628 Springer Science & Business Media, 1–735 pp., <https://doi.org/10.1007/978-1-4020-9508-5>, 2010.

629 Plank, S., Marchese, F., Genzano, N., Nolde, M., and Martinis, S.: The short life of the volcanic island
630 New Late'iki (Tonga) analyzed by multi-sensor remote sensing data, *Sci. Rep.*, 10, 22293,
631 <https://doi.org/10.1038/s41598-020-79261-7>, 2020.

632 Rabinovich, A. B.: Spectral analysis of tsunami waves: Separation of source and topography effects, *J.*
633 *Geophys. Res. Ocean.*, 102, 12663–12676, <https://doi.org/10.1029/97JC00479>, 1997.

634 Rabinovich, A. B.: Seiches and harbor oscillations. in: *Handbook of coastal and ocean engineering*, pp.
635 193–236, 2009.

636 Rabinovich, A. B., Thomson, A. E. R. E., and Stephenson, F. E.: The Sumatra tsunami of 26 December
637 2004 as observed in the North Pacific and North Atlantic oceans, *Surv. Geophys.*, 27, 647–677,
638 <https://doi.org/10.1007/s10712-006-9000-9>, 2006.

639 Rabinovich, A. B., Titov, V. V., Moore, C. W., and Eble, M. C.: The 2004 Sumatra Tsunami in the
640 Southeastern Pacific Ocean: New Global Insight From Observations and Modeling, *J. Geophys. Res.*
641 *Ocean.*, 122, 7992–8019, <https://doi.org/10.1002/2017JC013078>, 2017.

642 Ramalho, R. S., Winckler, G., Madeira, J., Helffrich, G. R., Hipólito, A., Quartau, R., Adena, K., and
643 Schaefer, J. M.: Hazard potential of volcanic flank collapses raised by new megatsunami evidence, *Sci.*

644 Adv., 1, e1500456, <https://doi.org/10.1126/sciadv.1500456>, 2015.

645 Ramírez-Herrera, M. T., Coca, O., and Vargas-Espinosa, V.: Tsunami Effects on the Coast of Mexico

646 by the Hunga Tonga-Hunga Ha'apai Volcano, *Pure Appl. Geophys.*, <https://doi.org/10.1007/s00024-022-03017-9>, 2022.

647

648 Satake, K.: Earthquakes: Double trouble at Tonga, *Nature*, 466, 931–932,

649 <https://doi.org/10.1038/466931a>, 2010.

650 Satake, K., Heidarzadeh, M., Quiroz, M., and Cienfuegos, R.: History and features of trans-oceanic

651 tsunamis and implications for paleo-tsunami studies, *Earth-Science Rev.*, 202, 103112,

652 <https://doi.org/10.1016/j.earscirev.2020.103112>, 2020.

653 Self, S. and Rampino, M. R.: K-1981Self_Nature_The 1883 eruption of Krakatau, *Nature*, 294, 699–

654 704, <https://doi.org/10.1038/294699a0>, 1981.

655 Stern, S., Cronin, S., Ribo, M., Barker, S., Brenna, M., Smith, I. E. M., Ford, M., Kula, T., and

656 Vaiomounga, R.: Post-2015 caldera morphology of the Hunga Tonga-Hunga Ha'apai caldera,

657 Tonga, through drone photogrammetry and summit area bathymetry, *EGU Gen. Assem.* 2022,

658 <https://doi.org/10.5194/egusphere-egu22-13586>, 2022.

659 Themens, D. R., Watson, C., Žagar, N., Vasylkevych, S., Elvidge, S., McCaffrey, A., Prikryl, P., Reid,

660 B., Wood, A., and Jayachandran, P. T.: Global Propagation of Ionospheric Disturbances Associated

661 With the 2022 Tonga Volcanic Eruption, *Geophys. Res. Lett.*, 49, e2022GL098158,

662 <https://doi.org/10.1029/2022GL098158>, 2022.

663 Thomson, R. E. and Emery, W. J.: *Data Analysis Methods in Physical Oceanography*: Third Edition,

664 New York: Elsevier, 1–716 pp., 2014.

665 Titov, V., Rabinovich, A. B., Mofjeld, H. O., Thomson, R. E., and González, F. I.: The Global Reach of

666 the 26 December 2004 Sumatra Tsunami, *Science* (80-.), 309, 2045–2049,

667 <https://doi.org/10.1126/science.1114576>, 2005.

668 USGS: M 5.8 Volcanic Eruption - 68 km NNW of Nuku'alofa, Tonga, U.S. Geol. Surv., 2022.

669 Wang, Y., Heidarzadeh, M., Satake, K., Mulia, I. E., and Yamada, M.: A Tsunami Warning System

670 Based on Offshore Bottom Pressure Gauges and Data Assimilation for Crete Island in the Eastern

671 Mediterranean Basin, *J. Geophys. Res. Solid Earth*, 125, e2020JB020293,

672 <https://doi.org/10.1029/2020JB020293>, 2020.

673 Wang, Y., Zamora, N., Quiroz, M., Satake, K., and Cienfuegos, R.: Tsunami Resonance
674 Characterization in Japan Due to Trans-Pacific Sources: Response on the Bay and Continental Shelf, J.
675 Geophys. Res. Ocean., 126, 1–16, <https://doi.org/10.1029/2020JC017037>, 2021.
676 Wang, Y., Heidarzadeh, M., Satake, K., and Hu, G.: Characteristics of two tsunamis generated by
677 successive Mw 7.4 and Mw 8.1 earthquakes in Kermadec Islands on March 4, 2021, Nat. Hazards Earth
678 Syst. Sci., 22, 1–10, <https://doi.org/10.5194/nhess-2021-369>, 2022.
679 Watanabe, S., Hamilton, K., Sakazaki, T., and Nakano, M.: First Detection of the Pekeris Internal
680 Global Atmospheric Resonance: Evidence from the 2022 Tonga Eruption and from Global Reanalysis
681 Data, J. Atmos. Sci., 79, 3027–3043, <https://doi.org/10.1175/jas-d-22-0078.1>, 2022.
682 Yuen, D. A., Scruggs, M. A., Spera, F. J., Yingcai Zheng, Hao Hu, McNutt, S. R., Glenn Thompson,
683 Mandli, K., Keller, B. R., Wei, S. S., Peng, Z., Zhou, Z., Mulargia, F., and Tanioka1, Y.: Under the
684 Surface: Pressure-Induced Planetary-Scale Waves, Volcanic Lightning, and Gaseous Clouds Caused by
685 the Submarine Eruption of Hunga Tonga-Hunga Ha'apai Volcano Provide an Excellent Research
686 Opportunity, Earthq. Res. Adv., <https://doi.org/10.1016/j.eqrea.2022.100134>, 2022.
687 Zhang, S., Vierinen, J., Aa, E., Goncharenko, L. P., Erickson, P. J., Rideout, W., Coster, A. J., and
688 Spicher, A.: 2022 Tonga Volcanic Eruption Induced Global Propagation of Ionospheric Disturbances
689 via Lamb Waves, Front. Astron. Sp. Sci., 9, 1–10, <https://doi.org/10.3389/fspas.2022.871275>, 2022.
690